Buckling assessment of GFRP and carbon fiber-reinforced plastic filament-wound tubes using an acoustic emission-based methodology

Alimirzaei, Sajad; Ahmadi Najafabadi, Mehdi; Bani Mohammad Ali, Amir; Pahlavan, Lotfollah

Important note
To cite this publication, please use the final published version (if applicable).
Please check the document version above.

Buckling assessment of GFRP and carbon fiber-reinforced plastic filament-wound tubes using an acoustic emission-based methodology

Sajad Alimirzaei[1,2], Mehdi Ahmadi Najafabadi[1] ⓘ, Amir Bani Mohammad Ali[1] and Lotfollah Pahlavan[3]

Abstract
The aim of this research is to investigate the failure mechanisms of the filament-wound composite tubes under axial compressional loading by using an acoustic emission approach. First, the mechanical properties of ±45°C composite tubes were obtained experimentally. Then, failure due to the buckling phenomenon and crashworthiness characteristics were studied utilizing numerical simulation and experimental methods. Tubes were next simulated in ABAQUS software, and a continuum damage mechanics model was implemented in a progressive framework to assess the failure modes. From the macroscale view, results showed that the damage behavior of composite tubes turned out to be dominated by local buckling followed by a post-buckling field, which is generated by longitudinal cracks along the winding direction. On the micro-scale, the acoustic emission-based procedure based on the wavelet packet transform method was adopted. The hierarchical modeled assessment resulted in the identity of four clusters of AE signals. In GFRP tubes, the fiber breakage and fiber/matrix separation could mostly control the higher percentage of damage and cause to increase the energy absorption. Finally, by comparing the results obtained from micro and macro scales, the local buckling failure mode was attributed to the low content of fiber/matrix debonding in the structure.

Introduction

Cylindrical composite tubes have numerous applications in engineering structures, such as in aerospace, energy, aeronautic, automotive sector, and marine due to their excellent high specific strength and stiffness, and high corrosion strength.[1,2] Fiber-reinforced plastic (FRP) composites are widely used in energy-absorbing devices due to their high capacity to dissipate crash energy. Substantial efforts have been made to optimize the energy absorption capacity of FRP structures.[3,4] For the success of this process, damage mechanisms must be accurately identified and controlled during the production process. When composite structures are subjected to uniaxial load, as the load increases steadily, the composite cylindrical tube starts to deform stably. When the load achieves a critical point, the equilibrium phase transits into instability. If the composite tube is able to support a contribution of the load after buckling, post-buckling properties can be further exploited. Generally, the prediction of buckling in thin-walled structures is very complicated and not still fully understood, as it is highly

dependent on factors such as fabrication defects, stacking sequence and different loading,[5–9] mosaic pattern,[10] and geometrical parameters.[11,12] Tafreshi[13] expanded a numerical simulation model to predict the buckling and post-buckling behavior of composite tubes under axial load and external pressure. The results of this study showed that delamination was the main cause of the buckling. In other studies, researchers presented the effects of fiber orientation on the crushing modes,[14] absorbed energy in hybrid biaxial/uniaxial

[1]Department of Mechanical Engineering, Amirkabir University of Technology, Tehran, Iran
[2]Technologies Research Center (NTRC), Amirkabir University of Technology, Tehran, Iran
[3]Department of Maritime and Transport Technology, Delft University of Technology, Delft, The Netherlands

Corresponding author:
Mehdi Ahmadi Najafabadi, Department of Mechanical Engineering, Amirkabir University of Technology, 424 Hafez Ave, 15914, Tehran, 158754413, Iran.
Email: ahmadin@aut.ac.ir

braided composite tubes,[15] and the behavior of various ratios of axial to hoop stress[16] through linear and non-linear analysis. To calculate the linear and non-linear buckling responses of cylindrical tubes, computational tools based on analytical or numerical methods can be used. Among the extensive research related to the buckling of cylindrical tubes and considering the initial geometrical imperfection, we can refer to Donnell,[17] Riks,[18] Flügge,[19] Simitses,[20] and Wei et al.[21] Also, improved computational models that can more accurately predict the propagation of the damage in filament wound (FW) composites are important for understanding the characteristics of these structures.[22,23] For this purpose, the continuum damage mechanics (CDM) model has been proposed and demonstrated successfully.[24] Over the past decades, due to the limitations of the scanning electron microscopy (SEM) method[12,25] to characterize the different damage mechanisms, extensive research has been performed in the field of the acoustic emission (AE) technique[26–28] and digital image correlation (DIC) method.[29] For example, Oskouei et al.[30] utilized the AE technique to evaluate the fracture toughness of the glass/polyester composite laminates at the first mode of delamination. Fotouhi et al.[31] and Chandarana et al.[32] studied the behavior of the composite samples under the flexural test using the AE method. They used the fuzzy c-mean clustering technique to classify the damage mechanisms. Their results showed that the bands with low frequencies (around 140 kHz), mean frequency (around 265 kHz), and high frequency (around 412 kHz) belong to matrix cracking, fiber-matrix separation, and fiber breakage, respectively. Khalifa et al.[33] and Šofer et al.[34] utilized the AE to analyze the damage evolution and the various failures that occurred in composite tubes subjected to the tensile and three-point bending loads, respectively. They found the distinction between delamination and debonding relatively challenging due to the close frequency spectra. Use of the AE method is extremely beneficial in the failure identification, detection, and location of cracks.[35] For determining the size and location of this failure, Micro-CT and DIC test methods can be used. The DIC method allows us to assess the stress and strain field results of composite structures.[36,37] A quantitative assessment of each of the damage mechanisms can be of great help in understanding how energy is absorbed by the target structure, which could be used to optimize the structures based on the effective damage mechanism. Due to the limitations of eye inspection, SEM methods, and numerical methods, it seemed necessary to use a precise technique to gain more detailed insight into the damage mechanisms, the boundary between different damage mechanisms, and the effect of each damage mechanism on the energy absorption capacity of FW tubes. The focus of this study is to identify the failure mechanisms of ±45°C CFRP and GFRP composite tubes due to buckling phenomena employing the AE method to compare and optimize the damage mechanics for increasing the energy absorption capacity of the FW composites. To recognize the damage

mechanisms, the values of frequency, energy, and amplitude of the AE signals were used to investigate the failure in different regions of the force–displacement diagram. Then, using the machine learning based-method various damage mechanisms were characterized. Finally, the results were analyzed using a recognition approach based on the wavelet packet transform (WPT) model and fast Fourier transforms (FFT), and the percentage of damage mechanisms was obtained. Also, for progressive damage analysis of the tubes, the CDM model was written as a user material subroutine (UMAT) in Fortran software, and compiled by ABAQUS™ software. Finally, the surface morphology of fabricated tubes was examined, and DIC was utilized to obtain displacement/strain contours.

Experimental considerations

To investigate the acousto-mechanical behavior of ±45°C composite tubes under quasi-static compressional loading, carbon/epoxy, and glass/epoxy composite tubes were fabricated using an X-winder filament winding machine (Figures 1(a) and (b)). FW composite tubes were initially cured at room temperature for 24 h and then cured in an oven with air circulation at 100°C for 4 h. Finally, specimens (inner diameter of 60 mm × length 120 mm × wall thickness 1.5 mm) were cut from the original length (Figures 1(c) and (d)). Three replicated tests were performed to ensure experimental reliability, and photographs were taken by DIC cameras to monitor the crushing process history. In order to obtain the material properties for simulating the composite tubes in Abaqus software, at first, the mechanical properties test samples were made using the filament winding machine (Figure 2) and were tested according to ASTM D3039,[38] ASTM 3410M-03,[39] and ASTM D3518[40] standards (Figure 2(e)). The experimental samples included 0°, 90° (Figures 2(a) and (b)), and 45° (Figures 2(c) and (d)) specimens under tensile, compressive, and shear loading.[41] The tensile test was performed with a constant speed of 2 mm/min using 3 FW composite samples for each angle (Figure 2(f)). Also, the compressive strength was obtained using the compression test based on ASTM D3410M-03 standard using 3 samples for each angle (0° and 90°) with a speed of 1.3 mm/min. Finally, the shear properties were achieved via the geometric dimensions described in the ASTM D3518 standard.[41] In Table 1, the dimensions of the testing samples and used ASTM standard are shown.

To monitor the AE activity during the test, an eight-channel AE AMSY-6 and a Vallen System with a maximum sampling frequency of 40 MHz were used. The utilized AE sensors were broadband, single-crystal piezoelectric transducer (AE1045S-VS900M) with 34 dB external preamplifier and an operating frequency range of 100–900 kHz. To record the acoustic activity, two sensors were mounted by adhesive tape with an equal distance of 40 mm
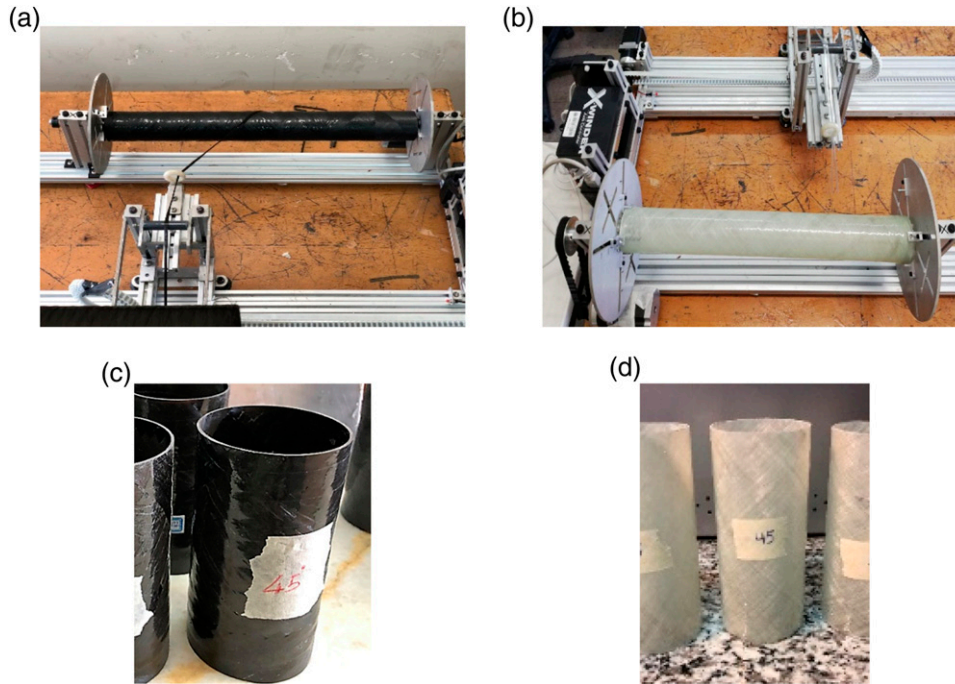
Figure 1. Fabrication of (a) CFRP composite tubes, (b) GFRP composite tubes, (c) CFRP FW composite tube, and (d) GFRP composite tube.

from the top and bottom of the tube. Silicon grease was used to provide good coupling between the specimen surface and the AE sensor. The sampling rate and the threshold were set to 2 MHz and 55 dB, respectively. A hit definition time (HDT) and hit lockout time (HLT) of both 200 μs were applied. Also, according to ASTM E976-10,[42] a pencil lead break was used for determining the reproducibility of acoustic sensors response. The experiments were performed at a temperature of 24°C at a crosshead speed of 5 mm/min throughout all the tests. The typical experimental setup of the axial compression testing of the composite tube is shown in Figure 3.

Acoustic emission analysis

To validate the AE technique, the features of the AE signals including AE energy, peak frequency, and cumulative AE energy are combined with mechanical data. Subsequently, the Sentry function[43] is utilized to process the signal. Then, using Hierarchical clustering methods, the AE data are classified. Finally, to calculate the energy of AE signals for each frequency interval, the WPT[44,45] was utilized. Based on this, a variable is defined that relates the duration of the AE signal to the rise time in the entire considered frequency domain and acoustic analysis is done based on it. Then, this parameter is used to filter the AE-originating signals for various failure mechanisms. To characterize the suitable

decomposition level, an entropy criterion is used, based on which the clusters were decomposed to up to three levels, and then divided into 8 parts.[45] Then, by using the power spectrum analysis in the FFT approach, the decomposition of each of these components was carried out. To calculate the energy level of each wavelet component, the following equation can be used[46]

$$E_j^i(t) = \sum_{\tau=t_0}^{t} \left(f_j^i(t) \right)^2 \tag{1}$$

$f_1^i, \ldots, f_j^i$ represent each of the Wavelet components for the *ith* level of decomposed signal and $E_1^i, \ldots, E_j^i$, show the amount of energy associated with each component. To calculate the total energy of the signal, the following equation is used

$$E_{total}(t) = c \sum_i \sum_j E_j^i(t) \tag{2}$$

Finally, the relative energy distribution at each level, p_j^i, is given by

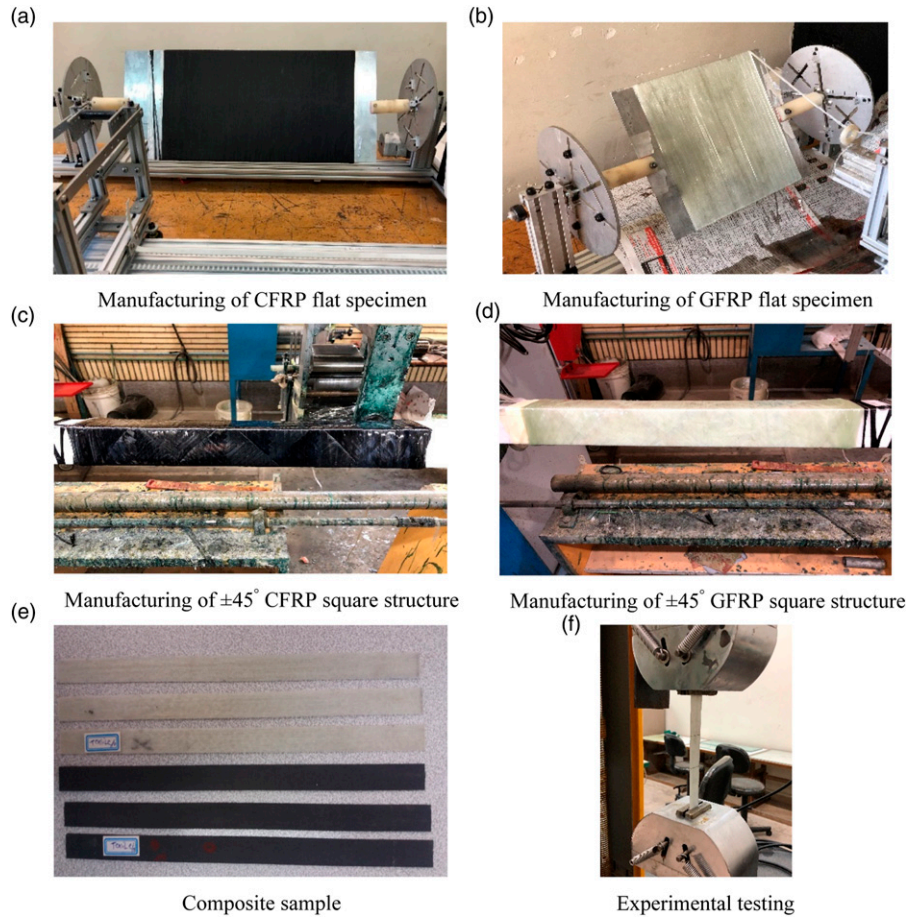$$p_j^i(t) = c \sum_i \sum_j \frac{E_j^i(t)}{E_{total}(t)} \tag{3}$$

Figure 2. A schematic of the fabrication and testing process of the FW composite specimens. (a) Manufacturing of CFRP flat specimen. (b) Manufacturing of GFRP flat specimen. (c) Manufacturing of ±45° CFRP square structure. (d) Manufacturing of ±45° GFRP square structure. (e) Composite sample. (f) Experimental testing.

Table 1. The dimensions of specimens for mechanical properties testing.

Experimental test	ASTM standard	Winding angle	Length*width (mm*mm)	Thickness (mm)	Properties and model parameters
Tensile test	ASTM3039	0	250*15	1.2	E_{11}, v_{12}, X_t
		90	175*25	1.2	E_{22}, d_2, Y_t
Compressive test	ASTM 3410M-03	0	150*10	1.2	$X_{C_0}, X_C, \sigma_{110}$
		90	150*25	1.2	$Y_C, \sigma_{220}, E_{Dc}$
Shear test	ASTM D3518	45	250*25	1.45	$G_{12}, S_{12}, d_6, S_{12y}$

Hierarchical classification clustering method

The technique starts with considering each data point as a united cluster and calculating the distance between each of the two clusters. Using the hierarchical algorithm, two nearest clusters are found and a new cluster is created containing all data points of the two clusters. In the following, the distance between the new cluster and the old one is calculated and the two closest clusters are merged again. This process is repeated until the desired number for the clusters is achieved.[27]

Numerical model

Carbon fiber-reinforced plastic (CFRP) tube and top and bottom plates were modeled by using conventional shell elements (S4R) with homogenous reduced integration and rigid body with quadrilateral elements (R3D4), respectively. Also, boundary conditions were applied to the upper and lower plate, according to Figure 4(a). Due to the convergence tests (Figure 4(b)), shell elements with an average size of 2 mm were found adequate for modeling.[25]
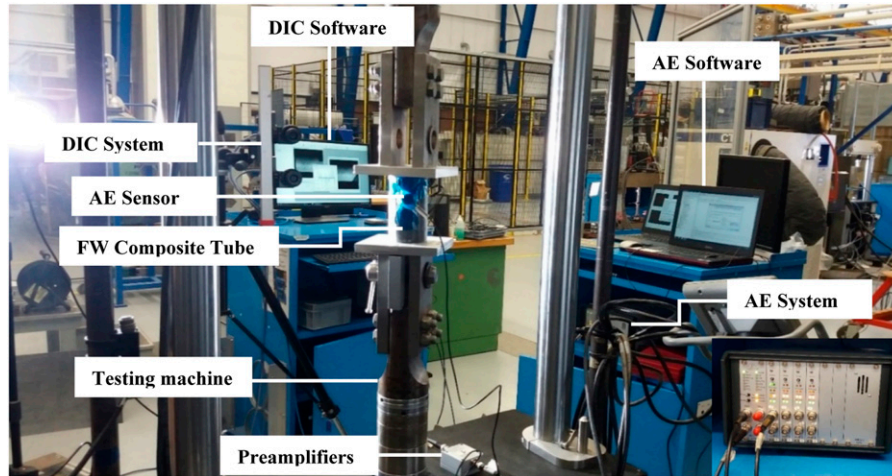
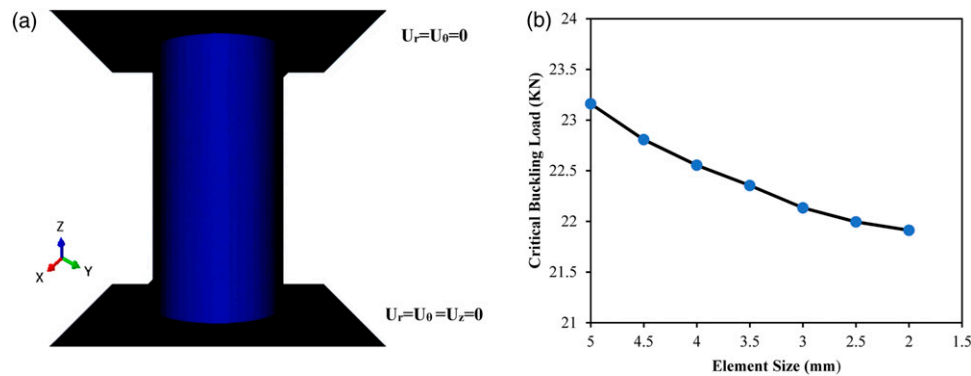**Figure 3.** Experimental setup of this study.

Figure 4. (a) Schematics of CFRP composite model in ABAQUS, (b) The convergence analysis.

Manufactured thin-walled composite tubes are never entirely smooth. They contain some irregularities on the surface of the column, which may decrease the compressive stability and lead to failure due to buckling. To introduce the initial imperfection of the shell into the FE model, the approach of linear buckling mode-shape imperfections (LBMI) proposed by Khot and Venkayya[47] was employed. This method applies a scaled factor of the linear buckling modes to the FE model and perturbs the nodal coordinates of the cylinder before the nonlinear analysis.[48] Based on testing results, it was observed that the best approach to create this defect is to utilize the linear combination of deformations in some first buckling modes. Due to the previous literature, by increasing the buckling force, the effect of buckling modes on creating geometric defects decreases, so the lowest buckling modes provide the most critical imperfections. By considering all these points, the imperfection was adopted by using the first, third, and fifth modes. Finally, by adding the modes coefficients by the *Imperfection option in ABAQUS software, the defects

were defined.[49] In Figure 5, the flowchart of the buckling analysis of the FW tube is shown.

Damage model

The properties of the composite tube depend on the behavior of each ply, including the damage mechanisms of the fibers and the matrix. Various criteria have been proposed for considering the damage mechanisms of the composite materials, and in this research, the mathematical formulations were developed using a mesoscale approach.[24,50] A subroutine was written based on the progressive failure analysis model as a UMAT in Fortran software, which was linked to ABAQUS software. Figure 6 presents the flowchart of UMAT and ABAQUS integration for progressive failure analysis.

In Table 2, a summary of damage criteria and degradation laws for the failure model is shown. A single-directional composite structure under tensile loading in the direction of fibers contains linear elastic properties. In this model, it is assumed that the tensile behavior of the
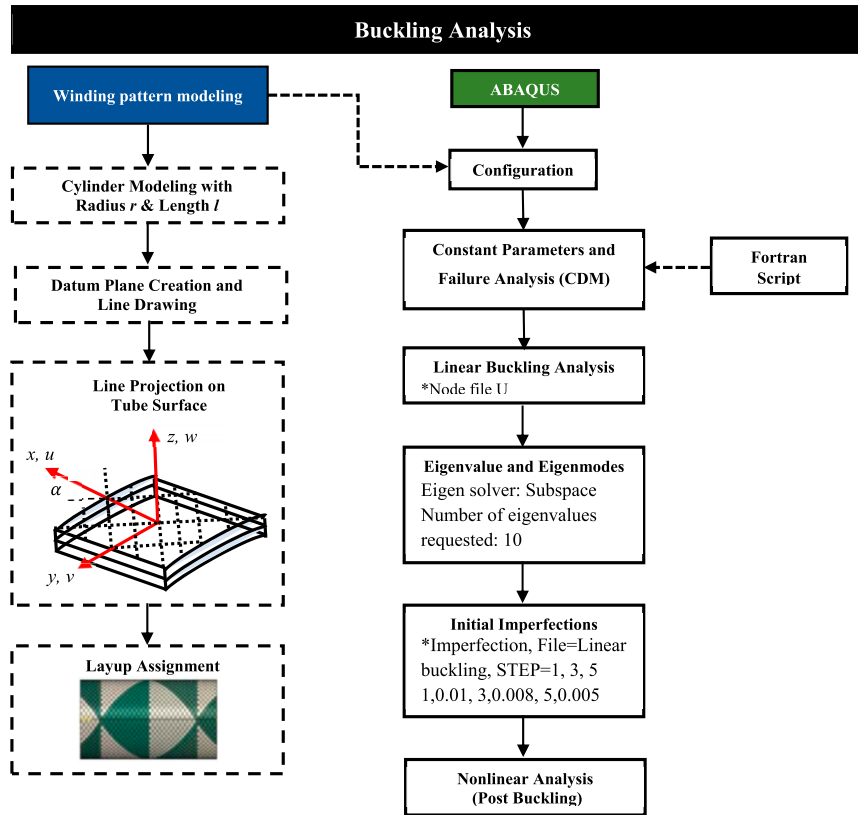
Figure 5. Simulation process for FW composite tube.

filament is not affected by the matrix damage. Hence, it utilizes the maximum stress criteria to detect damage in the fiber. While the behavior of fiber under the compressive longitudinal load changes linearly to a certain value. After that, a nonlinear elastic behavior is observed (Table 2: Equation (2)). So, any increase in the compressive load in the direction of the fibers would lead to creating a nonlinear elastic stress-strain behavior. To model the damage process in the matrix, two internal damage variables of d_2 (related to σ_{22}) and d_6 (related to τ_{12}) are utilized varying from zero for the undamaged materials to one for the completely damaged materials. In this case, the damage variables d_2 and d_6 are considered as a function of filament arrangement angle (θ) and thermodynamic forces (Y),[24,51] and, the parameters $A\,(\theta), B\,(\theta), C\,(\theta)$, and $D\,(\theta)$ are obtained using the empirical experiments and (Table 2: Equation (5)), the thermodynamic forces are obtained using the strain energy density of the damage.[24,52]

Results and discussion

Mechanical results

After performing experimental testing, the mechanical properties of the filament wound composite samples were obtained according to Table 3.

In Figure 7, the load-displacement diagrams of three CFRP specimens subjected to the axial compression and the DIC deformation history were shown. As can be seen in Figure 7(a), it seems that in terms of mechanical properties, these curves are divided into three regions: The first, linear region, corresponds to the elastic behavior of composite tube. A second zone starts from the limit of the first zone: the curves become nonlinear and they suddenly drop. It seems that the reason for this sharp decline is due to the large difference between the fiber orientation and force direction which causes a decrease in the strength of the tube. In the third zone, the trend of loading increases slightly with advancing the displacement and leads to total damage. According to the deformation morphology of the composite tube, the damage initiates with matrix cracking and fiber-matrix debonding, however, since matrix cracking dominates the separation of fiber from the matrix, the composite tube could not be crushed from the top and bottom edge (Figure 7(b)). Consequently, due to the high shear stresses caused by the fracture, the cracks perpendicular to the fiber direction were inhibited effectively by the fibers, and the micro-cracks propagated along the fiber direction. Finally, the energy is absorbed by deformation close to the middle of the composite tube (Figure 7(c)), and local buckling occurs. It appears that in this region, failure occurred along with the plastic deformation through the thickness, and the deformation around the
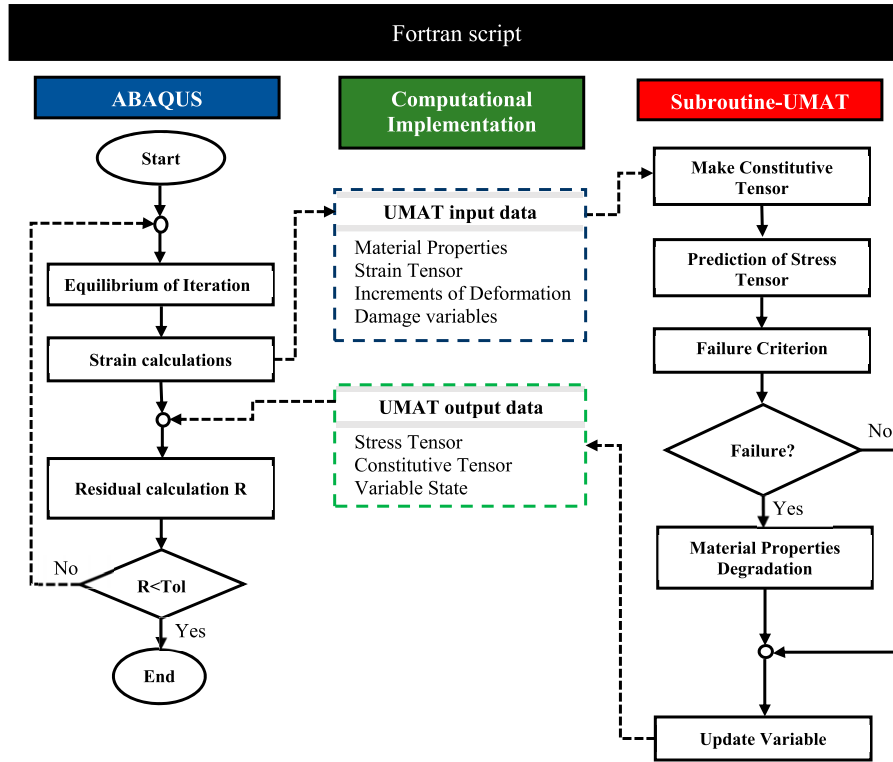
Figure 6. The flowchart of the continuous damage mechanics model.

Table 2. Summary of failure criteria and degradation laws for damage model.

Number	Loading type	Failure criteria	Degradation law
1	$\sigma_{11} \geq 0$	$\frac{\sigma_{11}}{X_T} \geq 1$	$E_{11} = 0$
2	$\sigma_{11} \leq 0$	$\frac{|\sigma_{11}|}{X_{C0}} \geq 1$	$E_{11} = \frac{X_{C0}}{|\varepsilon_{11}|}(1 - h(\varepsilon_{11})) + h(\varepsilon_{11})E_{110}$
3	$\sigma_{22} > 0, \sigma_{12} \neq 0$	$f \geq 0$	$d_2 = A(\theta)Y_2 + B(\theta)$
4	$\sigma_{22} < 0, \sigma_{12} \neq 0$	$f \geq 0$	$E_{22} = \frac{\sigma_{22y}}{|\varepsilon_{22}|}(1 - f(\varepsilon_{22})) + f(\varepsilon_{22})E_{220}$
5	$\sigma_{22} > 0, \sigma_{12} \neq 0$	$f \geq 0$	$d_6 = C(\theta)Y_6 + D(\theta)$

Table 3. Mechanical properties of CFRP and GFRP composite samples built by the filament winding method.

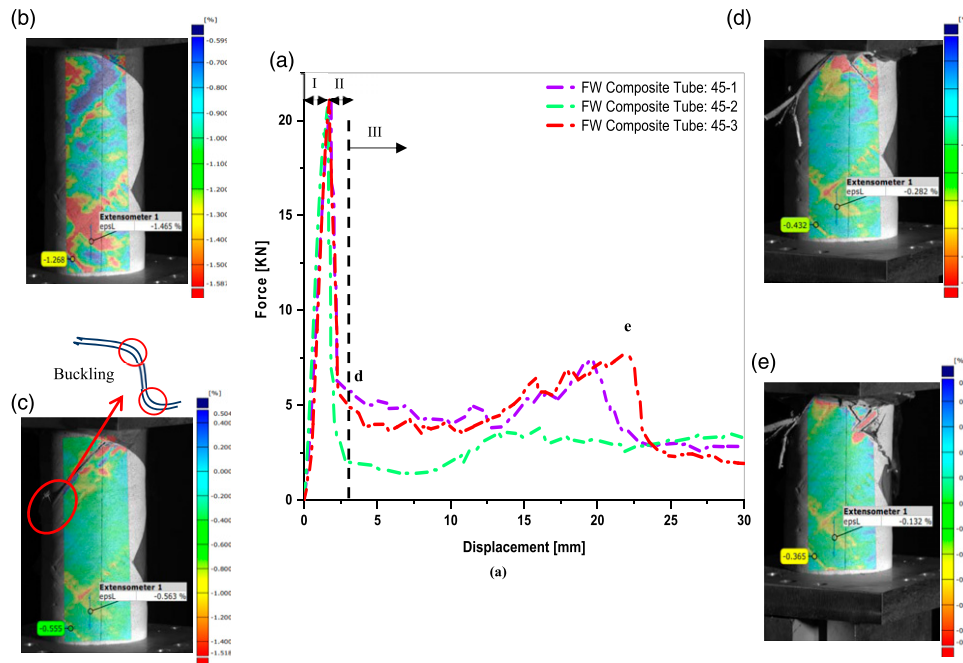| Parameter		CFRP	GFRP
Elastic properties	Longitudinal modulus E_{11} (GPa)	127.53	39
	Transverse modulus E_{22} (GPa)	8.76	8.6
	Shear modulus G_{12} (GPa)	3.84	3.8
	Poisson's ratio ν_{12}	0.3	0.28
	ν_{21}	0.021	0.062
Strength (MPa)	Longitudinal strength $\sigma_{1,t}$	1435.78	1080
	Transverse strength $\sigma_{2,t}$	45.38	39
	$\sigma_{1,c}$	613.9	620
	$\sigma_{2,c}$	139.57	128
	Shear strength τ_{12}	73.16	64

Figure 7. Displacement–force curves and deformation history of CFRP composite tube.

buckling area is in the elastic region. Also, on the convex side of the buckling region, the material is under tension, while the concave side is under compression. After buckling and severe force drop, with an increasing axial displacement, the damage gradually grows (Figure 7(d)), and with the extension of failure, the force decreases (Figure 7(e)). By more closely examining the curves, more areas appear in these diagrams and should be more accurately investigated by other indicators and methods.

There are several indexes to evaluate the crashworthiness of the composites. Energy absorption (EA), peak crushing force (PCF), mean crushing force, average stress, and crush force efficiency (CFE) are some of these indicators used for this purpose.[53] In Table 4, the failure behavior and mechanical properties of different specimens, and the crashworthiness indicators, are presented. As can be seen, the failure behavior for all specimens follows a similar trend, and there is good repeatability between the calculated indicators.

In the following, the results of the carbon/epoxy composite tube are compared with the results of the glass/epoxy composite tubes. According to the deformation history (Figure 8(a)) of the glass/epoxy composite tube, the damage begins with the fiber/matrix separation and the matrix cracking on the top edge. Then, with the propagation of the crack, local buckling occurred near the upper edge. While, in carbon/epoxy samples, with the propagation of cracks along the direction of the fibers, local buckling occurred close to the middle of the tube. According to Almeida et al.,[25] this type of failure occurs

due to the absence of adequate lateral stability, which could also generate micro-buckling. After the buckling zone, up to a displacement of 30 mm and a force of 3.17 kN, the load-displacement curve changes uniformly. Then, as the displacement increases, the force begins to increase, and the area under the curves increases. It seems that in the post-buckling stage, in the glass/epoxy sample, because of less displacement to reach the local failure site, the process of force increases occurs sooner due to the compaction of the material. By comparing the results of carbon/epoxy tubes with the glass/epoxy tubes (Figure 8(b)), it is concluded that the maximum force obtained for C-45 (21.05 kN) is 1.58 times of G-45 samples (13.30 kN), and the slope of the elastic region line of carbon/epoxy tubes is much higher than the glass/epoxy tubes. This fact indicates the higher modulus and high strength of carbon/epoxy samples than glass/epoxy samples. After the maximum load, the carbon/epoxy curve progresses uniformly and almost steadily, while the glass/epoxy curve begins to increase. Also, in both types of tubes, the drop part of the curves is similar and coincided. In Table 5, the crashworthiness indicators (Average value) of glass/epoxy FW composite tubes, are presented. As can be seen from this table, the mean force and absorbed energy are equal to 5.13 kN and 308.67 J, respectively. By comparing the carbon/epoxy sample with the glass/epoxy sample, up to a specific displacement of 40 mm, the energy absorption of the CFRP sample is higher (EA = 174.87 J) than the GFRP sample (EA = 171 J), but in the whole range of the crushing, it seems that the energy absorption of the glass/epoxy sample

Table 4. Experimental results for crushing indicators in CFRP tubes under quasi-static loading.

Specimen	PCF (KN)	$F_{mean} = \frac{EA}{d}$ (KN)	$CFE = \frac{F_{mean}}{PCF}$	$EA = \int_0^d F(x)dx$ (J)	Fracture displacement (mm)
C-45-1	21.22	4.91	0.23	150.08	1.84
C-45-2	20.82	3.48	0.17	105.49	1.58
C-45-3	21.10	4.85	0.23	148.49	1.72
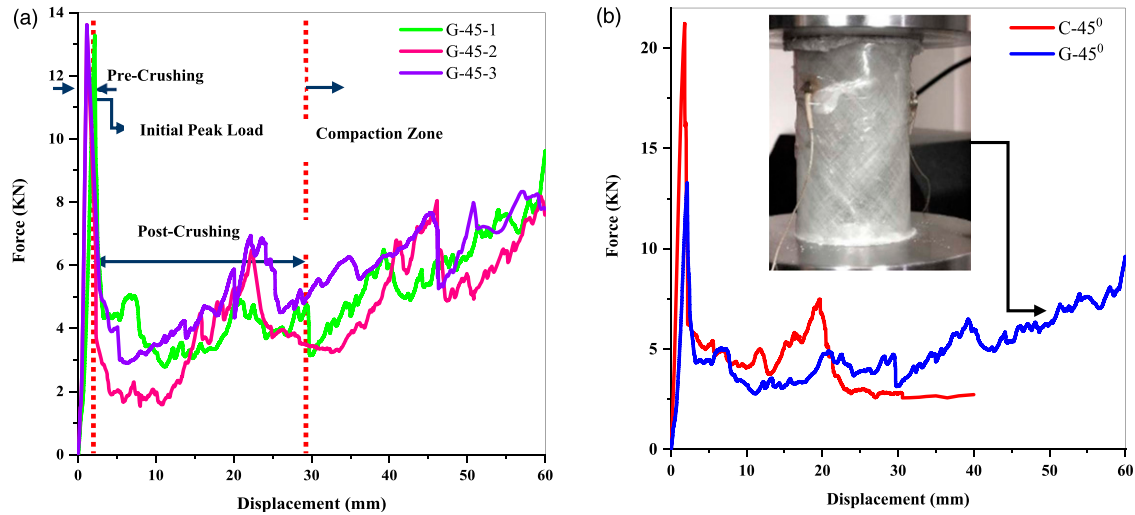
Figure 8. Displacement–force curves of (a) glass/epoxy composite tube, and (b) both types of FW composite tube.

Table 5. Crushing indicators of glass/epoxy composite tubes.

Specimen								
Average	PCF (KN)	STD	F_{mean} (KN)	STD	EA (J)	STD	CFE	STD
G-45	13.3	0.23	5.13	0.09	308.67	28.16	0.38	0.27

is higher than the carbon/epoxy sample. Therefore, in practical cases, choosing a glass/epoxy composite tube is economically more affordable.

Acoustic emission results

To identify the damage mechanisms and propagation of the crack of the composite tubes, the analysis of AE signals was utilized. For this purpose, first, a statistical analysis based on a number of AE hits is performed to identify the best acquisition of signals and at the same time to identify the amplitude distribution range. Since different failure mechanisms may occur at different frequencies, the amplitude and energy parameters of the received signal were also investigated.[54] As can be seen from Figure 9, the analysis of signals indicated that the AE response of the carbon/epoxy composite tube to the loading includes five zones. In the first zone, which is limited to the value of 2.88% of axial displacement, no acoustic activity is received

in the FW composite tube, because no damage is recorded. The initiation of the second region is mostly accompanied by weak signals and a gradual increase in stress rate becomes evident in the specimen. By drawing a vertical line at this point, this vertical line intersects the horizontal axis at 0.86 mm. By further investigation with numerical and analytical methods, we realized that this point is equivalent to the bifurcation point created in the displacement-force diagram due to the buckling phenomena. Actually, there was a change in the system rigidity, and the concavity of the diagram changed at this point. At the start of this zone, the assessment of the frequency range of received signals shows that the energy level of these AE signals is very low and the range of its changes between 64–132 kHz, and seems to be related to the propagation of micro-cracks. When the force level increases, transverse cracking occurs in the matrix and grows in the fiber direction (Figure 7(c)). This region is mainly associated with an increase in cumulative AE energy and root mean squared (RMS) Voltage. At a displacement of
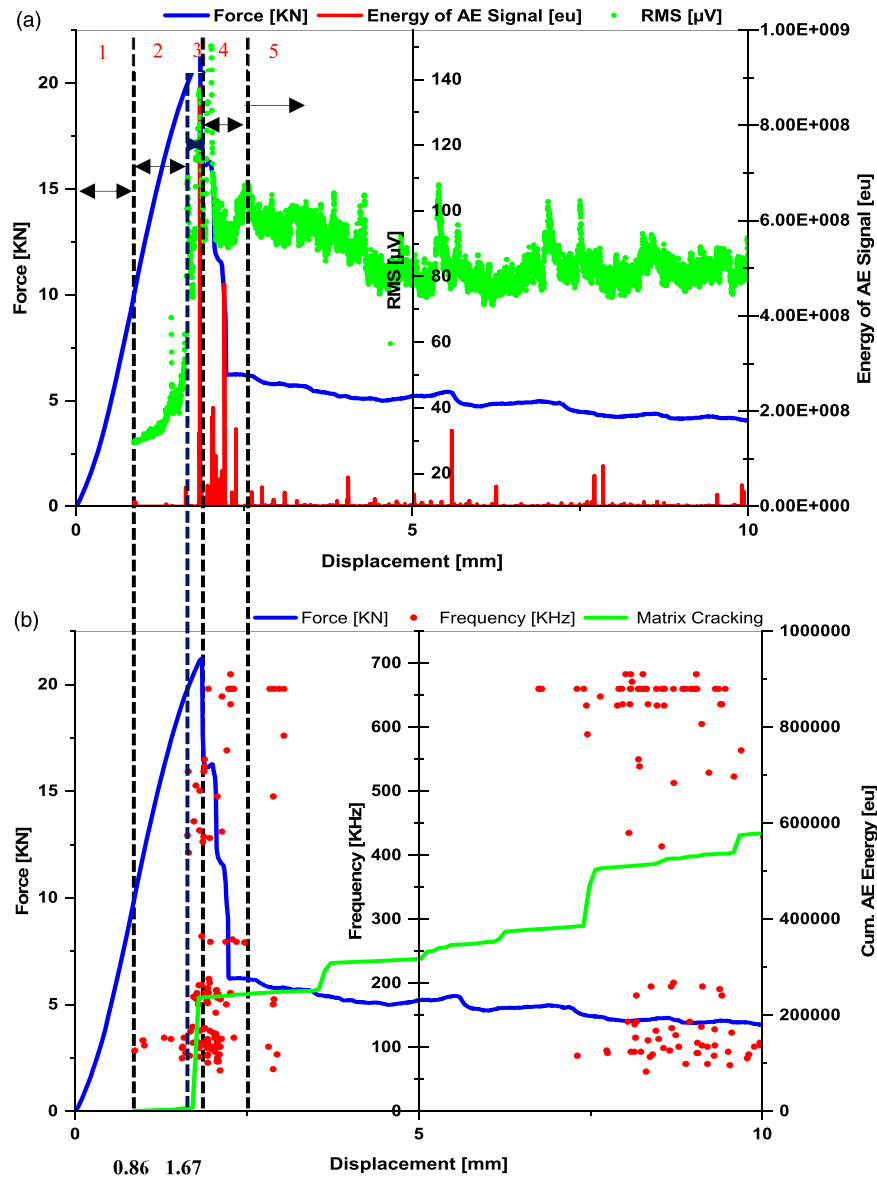
Figure 9. (a) Energy of AE signal and RMS Voltage with respect to the displacement, (b) Cumulative of AE energy for matrix cracking and frequency range of AE signals for CFRP composite tube.

Table 6. Characterization of the AE signal of FW composite specimens.

PCF = 21.218 Displacement = 1.841	Displacement (mm)	Load (N)	Percentage %
Propagation of micro-cracks	0.86	9.93	0.47
Fiber breakage	1.67	20.04	0.94
Fiber-matrix debonding	1.84	21.20	1

1.67 mm, in addition to crack growth in the matrix, signals in the frequency range of 404–531 kHz are received. These signals are related to the fiber breakage and this damage mechanism starts from this point. As the load reaches its peak value, severe changes in frequency happen in the range

of 64–201 kHz, and, the level of energy released due to the failure mechanisms increases sharply (maximum AE energy is 8.79 × 10⁸ eu) and the force suddenly decreases. At the beginning of this area, in addition to matrix cracking and fiber breakage, a new level of the signal appears at

a frequency of 271 kHz, which is related to the crack propagation in the fiber/matrix interface. The fourth region is mainly accompanied by an increase in cumulative AE events, and new frequency changes happened within the range of 248–273 kHz, that related to signals of the separation of fiber from the matrix. Finally, the fifth region starts, and the most obvious and strongest signals are related to matrix cracking and fibers breakage. While to the end of the elastic zone, the FW composite tube tends to suddenly lose integrity, without any significant warning phase, in region 5 tends to gradually continue with the accumulation of the AE events and gradual release of the AE energy. It is noteworthy that this region consists of various failures, and to accurately separate these signals, the effects of other parameters on the detection of the signal must be carefully considered. So, as can be seen from Table 6, the first indication of the propagation of micro-cracks and fiber breakage appears at 47% and 94%, of the maximum force, respectively.

To characterize the damage mechanisms bands of AE signals, that are based on the peak frequency and amplitude, the hierarchical[27] procedure was applied. According to Figure 10, the utilized modeled assessment analysis resulted in the identity of four clusters. The signals related to the first cluster are specified by an amplitude range of 41–84 dB,
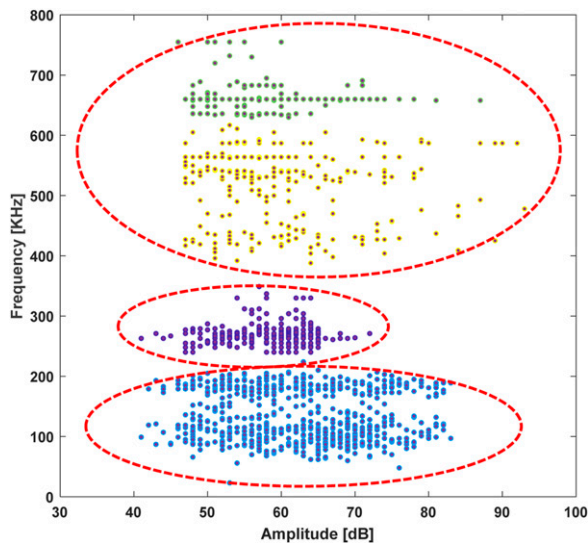

Figure 10. Classification of the acoustic data with the hierarchical method for CFRP composite tube.

with frequencies from 54 to 224 kHz. The second cluster was specified by the amplitudes mostly below 70 dB, and the frequency in the 240–349 kHz range. The third cluster is shown by the signals with an amplitude range of 48–81 dB, and the frequency in the 388–611 kHz interval. Finally, the fourth cluster is specified by the signals in the 48–81 dB amplitude range, and the frequency in the 630–700 kHz range. As can be seen from Table 7, these data are in agreement with the existing research.

AE data are used for health monitoring and are primarily qualitative. On the other hand, mechanical data are used to obtain a quantitative index of material behavior. To study the behavior of composite specimens with more detail, it is necessary to introduce a function examining the specimen's behavior qualitatively and quantitatively. The sentry function is introduced for this purpose and depends on the material strain energy and the energy of the AE signals during the experimental test. According to equation (4), the function is determined as the ratio of mechanical to acoustic energy[43]

$$f(x) = Ln\left[\frac{E_M(x)}{E_{AE}(x)}\right] \qquad (4)$$

where x is the test variable, $E_M(x)$ is the strain energy, and $E_{AE}(x)$ is the energy of the AE signals. In this equation, the sentry function is expressed by a combination of the four functions which is defined as follows: (a) incremental function, $P_1(x)$; (b) abrupt drop function, $P_2(x)$; (c) Constant function, $P_3(x)$; and (d) decreasing function, $P_4(x)$. As can be seen from Figure 11, at the beginning of loading, the strain energy stored in the structure is much higher than the AE, which makes the function have an ascending path. As the AE activities begin in the composite tube, the strain energy is gradually reduced and the AE energy increases. By activating extensive damage, the first sudden drop happens in the curve $P_2(x)$, which corresponds to matrix cracking. At a displacement of 2.08 mm, the sentry function curve decreases, which represents that the acoustic energy is higher than the mechanical energy $P_4(x)$. Finally, with the increases in the displacement to 8.9 mm, the sentry function shows a smooth behavior $P_3(x)$, which represents an equilibrium between AE energy and strain energy. As can be seen from these curves, the sentry function exhibits fairly good consistency with the failure behavior of the composite tube, which could indicate the accuracy of the AE results.

Table 7. Classification of the acoustic data in other researches.

Reference		Matrix cracking	Delamination	Debonding	Fiber breakage
[27]	Frequency range (kHz)	100–250	250–350	Near 300	300–700
	Amplitude range (dB)	30–40 and 40–80	>70	<60	50–100
[34]	Frequency range (kHz)	20–400	30–400	120–360	50–500
	Amplitude range (dB)	60–100	45–65	60–95	<60

Wavelet analysis

The frequency and energy analysis of the AE signals is beside the exploited assessment method, a relatively effective tool for filtering the AE signal, which can be related to various damage mechanisms. Based on this, a variable is defined that relates the duration of the AE signal to the rise time in the entire considered frequency domain and acoustic analysis is done based on it. Then, this parameter is used to filter the AE originating signals for various failure mechanisms. To do so, a WPT conversion program was written in MATLAB. In Figure 12, the FFT components and energy distributions of the third-level components of the carbon/epoxy composite tube are shown. According to the
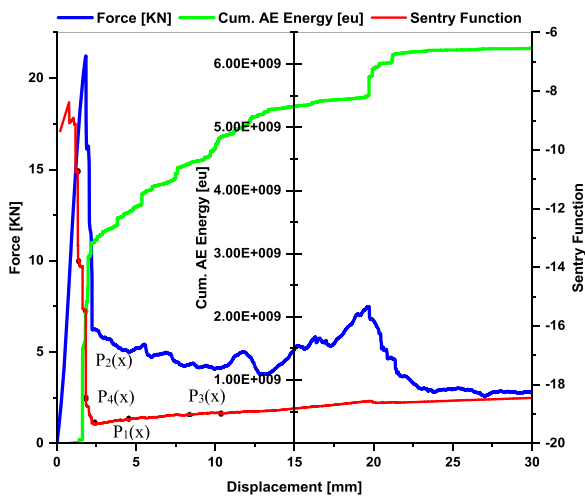
frequency range of eight components resulting from the decomposition of AE signals as well as the frequency range of matrix crack, fiber/matrix separation, and fiber breakage, the second and third components were dedicated to matrix crack (50–260 kHz and 120–310 kHz), where the amplitudes range of this damage mechanism was below 84 dB. Also, the fourth and fifth components, and the sixth, seventh, and eighth components were assigned to separation between plies from the matrix and fiber breakage, respectively. Then, using energy criteria (Figure 12(b)), the percentage of the signals in each component was determined. In Table 8, the percentage of failure mechanisms for glass/epoxy and carbon/epoxy composite samples were shown. According to this Table, the highest and lowest percentage of failure mechanism generated in the axial compression load process is related to the matrix cracking (71.17%), and fiber-matrix debonding (6.43%) process, respectively. Also, the percentage of fiber breakage was 22.40%. As can be observed, the percentage of failure mechanism of fiber/matrix debonding and fiber failure for glass/epoxy composite tubes is higher than the carbon/epoxy composite tubes. Therefore, it seems that the separation of fibers from the matrix and the fiber breakage was a significant effect on increasing the energy absorption of the glass/epoxy tubes than the carbon/epoxy tubes.

Simulation results

In Figure 13(a), the load-displacement curve of the numerical method (nonlinear buckling analyses) is shown. For obtaining the critical buckling load with the analytical method, by solving the eigenvalue problem of the algebraic equation the buckling equation of the composite tube is obtained
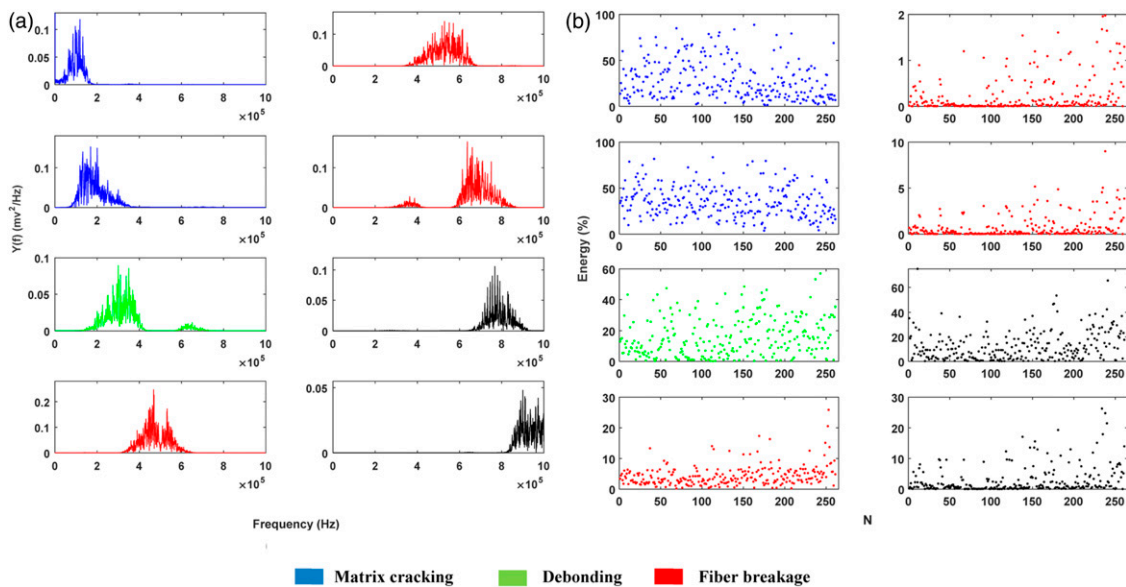

Figure 11. Sentry function behavior of carbon/epoxy FW composite tube.

Figure 12. (a) Fast Fourier Transform, and (b) Energy distribution results, of the 3rd level WPT components.

Table 8. The percentage of damage mechanisms for GFRP and CFRP tubes.

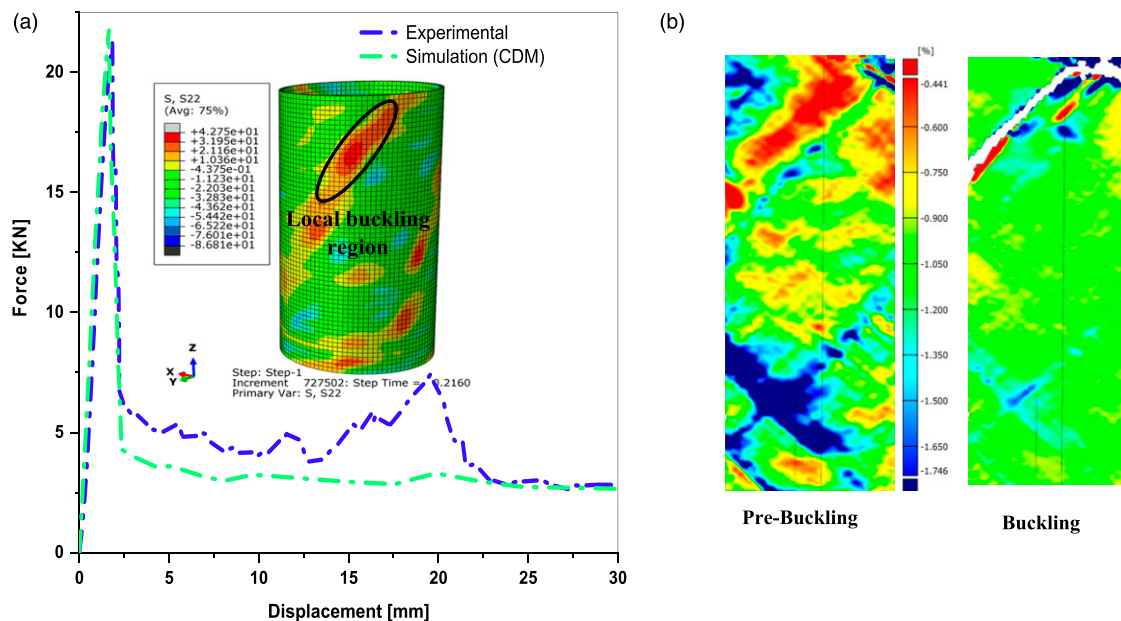| Sample type			
Percentage of damage mechanism (%)	Matrix cracking	Fiber/matrix debonding	Fiber breakage
GFRP-45	50.81	16.63	32.56
CFRP-45	71.17	6.433	22.397

Figure 13. (a) Load-displacement curves of FW CFRP composite tube for experimental and numerical methods, and (b) Longitudinal strain evaluated by DIC.

according to the literature.[25] In Table 9, the results of the numerical simulation and experimental testing of carbon/epoxy and glass/epoxy tubes are shown. As can be observed from this Table, both numerical simulation and experimental testing results acceptably predict the buckling loads. Also, the numerical simulation results for the post-buckling region show the same behavior as the experimental test results and are in good agreement with it. According to Figure 13(a), the results of simulation stress distribution indicated that the cracks propagate in the fiber direction, and due to local buckling occurring, the composite tube failed. Also, the 2D DIC strain contours of the composite tube at the moment of pre-buckling and buckling are displayed in Figure 13(b). As can be observed from this figure, in the pre-buckling zone, at the moment of lowering the upper fixture, the strain contours indicate the maximum compressive strain in the fiber direction on the top surface. By comparing the intensity of the deformation created in numerical simulation with the DIC technique (Figure 13(a)), the crack propagation process in both approaches is similar and there is a good

Table 9. Quantitative comparison of critical buckling load for CFRP and GFRP composite tube.

FW composite tube		PCF (KN)	EA (J)	F_{mean} (KN)
CFRP-1	Experimental	21.22	150.08	4.91
	Numerical	21.91	120.49	3.93
	Error (%)	3.15	24.56	24.93
GFRP-1	Experimental	13.24	302	5.09
	Numerical	13.82	253.54	4.23
	Error (%)	4.2	19.11	20.33

agreement between them. Then, sudden changes occur in the strain gradient, and displacement discontinuity is observed in the longitudinal direction of the composite tube.

Conclusion

Using data from the axial compressive tests the performance of the FW composite tube in terms of the failure mechanism's ability of energy absorption was investigated with AE

monitoring and numerical simulation. From the macroscale view, experimental results revealed that the failure mechanisms are generated by longitudinal cracks along the winding direction due to the plastic deformation in the buckling region. In the carbon/epoxy composite tube, at the elastic region, the stiffness change was happening near the load of 9.93 KN and displacement of 0.86 mm, and the concavity of the curve changed at this point, which coincides with the bifurcation point. When the force level increases, transverse cracking grows in the fiber direction and at a displacement of 1.67 mm, in addition, to crack growth in the matrix, signals in the frequency range of 404–531 kHz (fiber breakage) are received. Then, the AE events were increased, and new frequency changes happened within the range of 248–273 kHz (debonding). The signals related to the first, second, third, and fourth clusters were characterized by amplitude ranges of 41–84 dB, below 70 dB, and 48–81 dB. The results of the WPT showed that the highest and lowest percentage of damage mechanism is related to matrix cracking (71.17%) and fiber/matrix debonding (6.43%). Comparing the results obtained from micro and macro scales, the local buckling failure mode was attributed to the low content of fiber/matrix debonding. By comparing the results of two types of carbon/epoxy and glass/epoxy composite tubes we found that, in the glass/epoxy tubes, the fiber/matrix separation and the fiber breakage increases, and the contribution percentage of matrix cracking decreases. Finally, the results of the FE analysis and the results of the experimental test indicated that the difference between the experimental result with the analytical, and simulation results for critical buckling load were 4.02% and 3.15%, respectively.

Declaration of conflicting interests

Funding

ORCID iD

Mehdi Ahmadi Najafabadi https://orcid.org/0000-0001-9943-2644

References

1. Kollar LP and Springer GS. *Mechanics of composite structures*. New York, USA: Cambridge University Press, 2003.
2. Azeem M, Ya HH, Kumar M, et al. Application of filament winding technology in composite pressure vessels and challenges: a review. *J. Energy Storage* 2022; 49: 103468.
3. Ha NS and Lu G. Thin-walled corrugated structures: a review of crashworthiness designs and energy absorption characteristics. *Thin-Walled Struct* 2020; 157: 106995.
4. Ribeiro ML, Vandepitte D and Tita V. Experimental analysis of transverse impact loading on composite cylinders. *Compos. Struct* 2015; 133: 547–563.
5. Almeida JHS, Jr, Bittrich L, Jansen E, et al. Buckling optimization of composite cylinders for axial compression: a design methodology considering a variable-axial fiber layout. *Compos. Struct* 2019; 222: 110928.
6. Almeida JHS, Jr, Ribeiro ML, Tita V, et al. Damage and failure in carbon/epoxy filament wound composite tubes under external pressure: experimental and numerical approaches. *Mater & Des* 2016; 96: 431–438.
7. Almeida JHS, Jr, Ribeiro ML, Tita V, et al. Buckling and post-buckling in filament wound composite tubes under transverse compression. In: Proceedings of the 20th international conference on composite materials, Copenhagen, Denmark, 19–24 July 2015. Denmark MCI Scandinavia, 2015; 1–10.
8. Stedile Filho P, Almeida JHS, Jr and Amico SC. Carbon/epoxy filament wound composite drive shafts under torsion and compression. *J. Compos. Mater* 2018; 52: 1103–1111.
9. Maziz A, Tarfaoui M, Gemi L, et al. A progressive damage model for pressurized filament-wound hybrid composite pipe under low-velocity impact. *Compos. Struct* 2021; 276: 114520.
10. Azevedo CB, Almeida JHS, Jr, Flores HF, et al. Influence of mosaic pattern on hygrothermally-aged filament wound composite cylinders under axial compression. *J. Compos. Mater* 2020; 54: 2651–2659.
11. Tarafdar A, Razmkhah O, Ahmadi H, et al. Effect of layering layout on the energy absorbance of bamboo-inspired tubular composites. *J. Reinf. Plast. Compos* 2022; 41: 07316844211063865.
12. Gemi DS, Şahin ÖS and Gemi L. Experimental investigation of axial compression behavior after low velocity impact of glass fiber reinforced filament wound pipes with different diameter. *Compos. Struct* 2022; 280: 114929.
13. Tafreshi A. Efficient modelling of delamination buckling in composite cylindrical shells under axial compression. *Compos. Struct* 2004; 64: 511–520.
14. Hu D, Zhang C, Ma X, et al. Effect of fiber orientation on energy absorption characteristics of glass cloth/epoxy composite tubes under axial quasi-static and impact crushing condition. *Compos. Part A: Appl. Sci. Manuf* 2016; 90: 489–501.
15. Shi L, Wu Z, Cheng X, et al. Transverse impact response of hybrid biaxial/uniaxial braided composite tubes. *Eng. Struct* 2021; 244: 112816.
16. Carroll M, Ellyin F, Kujawski D, et al. The rate-dependent behaviour of $\pm 55°$ filament-wound glass-fibre/epoxy tubes under biaxial loading. *Compos Sci Technol* 1995; 55: 391–403.
17. Donnell LH. *Stability of thin-walled tubes under torsion*. California, USA, 1935.
18. Riks E. An incremental approach to the solution of snapping and buckling problems. *Int. J. Solids Struct* 1979; 15: 529–551.
19. Flügge W. *Stresses in shells*. Stanford University, USA: Springer Science & Business Media, 2013.
20. Simitses GJ. Buckling of moderately thick laminated cylindrical shells: a review. *Compos. Part B: Eng* 1996; 27: 581–587.
21. Wei R, Pan G, Jiang J, et al. Influence of ply angle and length on buckling behavior of composite shells under hydrostatic pressure. *J. Reinf. Plast. Compos* 2019; 38: 478–491.

22. Mindermann P and Gresser GT. Adaptive winding pin and hooking capacity model for coreless filament winding. *J. Reinf. Plast. Compos* 2022; 42: 07316844221094777.

23. Alimirzaei S, Ahmadi Najafabadi M, Nikbakht A, et al. Investigation of energy absorption capacity of 3D filament wound composite tubes: experimental evaluation, numerical simulation, and acoustic emission monitoring. *Mech. Adv. Mater. Struct* 2023; 1–16, doi:10.1080/15376494.2022.2163437.

24. Ribeiro ML, Tita V and Vandepitte D. A new damage model for composite laminates. *Compos. Struct* 2012; 94: 635–642.

25. Almeida JHS, Jr, Tonatto ML, Ribeiro ML, et al. Buckling and post-buckling of filament wound composite tubes under axial compression: linear, nonlinear, damage and experimental analyses. *Compos. Part B: Eng* 2018; 149: 227–239.

26. Alimirzaei S, Najafabadi MA and Khodaei A. Characterization of the damage mechanism of glass/epoxy composite tubes under quasi-static axial loading using acoustic emission monitoring. *Appl. Comp. Mater* 2022; 29: 1911–1936.

27. Saeedifar M and Zarouchas D. Damage characterization of laminated composites using acoustic emission: a review. *Compos. Part B: Eng* 2020; 195: 108039.

28. Alimirzaei S, Najafabadi MA, Nikbakht A, et al. Damage mechanism characterization of $\pm 35^{\circ}$ and $\pm 55^{\circ}$ FW composite tubes using acoustic emission method. *Int. J. Damage Mech* 2022; 31: 1230–1253.

29. Patel J, Ayyar A and Peralta P. Kink band evolution in polymer matrix composites under bending: a digital image correlation study. *J. Reinf. Plast. Compos* 2020; 39: 852–866.

30. Oskouei AR, Zucchelli A, Ahmadi M, et al. An integrated approach based on acoustic emission and mechanical information to evaluate the delamination fracture toughness at mode I in composite laminate. *Mater. Des* 2011; 32: 1444–1455.

31. Mohamad F, Hossein H, Farzad P, et al. Composite materials damage characterization under quasi-static 3-point bending test using fuzzy C-means clustering. *Appl. Mech. Mater* 2012; 110-116: 1221–1228.

32. Chandarana N, Soutis C and Gresil M. Damage detection in composite pipes during mechanical three point bending. In: International Workshop on Structural Health Monitoring (IWSHM) 2017, Stanford, USA. DEStech Publications, Inc, 2017; 1429–1436.

33. Khalifa AB, Zidi M and Abdelwahed L. Mechanical characterization of glass/vinylester ± 55 filament wound pipes by acoustic emission under axial monotonic loading. *C. R. Mec* 2012; 340: 453–460.

34. Šofer M, Cienciala J, Fusek M, et al. Damage analysis of composite CFRP tubes using acoustic emission monitoring and pattern recognition approach. *J. Mater* 2021; 14: 786.

35. Mohammadi R, Saeedifar M, Toudeshky HH, et al. Prediction of delamination growth in carbon/epoxy composites using a novel acoustic emission-based approach. *J. Reinf. Plast. Compos* 2015; 34: 868–878.

36. Almeida JHS, Jr, St-Pierre L, Wang Z, et al. Design, modeling, optimization, manufacturing and testing of variable-angle filament-wound cylinders. *Compos. Part B: Eng* 2021; 225: 109224.

37. Castro SG, Almeida JHS, Jr, St-Pierre L, et al. Measuring geometric imperfections of variable–angle filament–wound cylinders with a simple digital image correlation setup. *Compos. Struct* 2021; 276: 114497.

38. ASTM D3039. *Standard test method for tensile properties of polymer matrix composite materials*. West Conshohocken, PA, USA: Annual book of STM standards, 2008, 14.02.

39. ASTM D3410M-03. *Standard test methods for compressive properties of polymer matrix composite materials with unsupported gage section by shear loading*. West Conshohocken, PA, USA: Annual Book of ASTM Standards, 2008, 08.01.

40. ASTM 3518/D3518M-94. *Standard test method for in-plane shear response of polymer matrix composite materials by tensile test of a ±45 o laminate*. West Conshohocken, PA, USA: Annual Book of ASTM Standards, 2001, 15.

41. Alimirzaei S, Najafabadi MA and Nikbakht A. Investigation of mechanical properties and failure behavior of CFRP filament-wound composites using an acoustic emission-based methodology and numerical simulation. *Fibers Polym* 2022; 24(2): 693–707.

42. ASTM E976-10. *Standard guide for determining the reproducibility of acoustic emission sensor response*, West Conshohocken, PA: ASTM International, 2015; 03.03: 7.

43. Sobhani A, Saeedifar M, Najafabadi MA, et al. The study of buckling and post-buckling behavior of laminated composites consisting multiple delaminations using acoustic emission. *Thin-Walled Struct* 2018; 127: 145–156.

44. Barik T and Pal K. Prediction of drilled hole quality in bi-directional woven carbon fiber reinforced plastic using wavelet packets of force–torque signals. *J. Reinf. Plast. Compos* 2021; 40: 800–826.

45. Ali ABM, Alimirzaei S and Ahmadi Najafabadi M. Evaluation of damage of filament wound composite tubes under lateral loading by acoustic emission method and finite element simulation. *Modares Mechanical Engineering* 2022; 22: 647–655.

46. Barile C, Casavola C, Pappalettera G, et al. Detection of damage in CFRP by wavelet packet transform and empirical mode decomposition: an hybrid approach. *Appl. Comp. Mater* 2020; 27: 641–655.

47. Khot N and Venkayya V. *Effect of fiber orientation on initial postbuckling behavior and imperfection sensitivity of composite cylindrical shells*. United States Air Force: Air Force Flight Dynamic Lab Wright-Patterson AFB OH, 1970.

48. Shirkavand A, Taheri-Behrooz F and Omidi M. Orientation and size effect of a rectangle cutout on the buckling of composite cylinders. *Aerosp. Sci. Technol* 2019; 87: 488–497.

49. Ke Chun S and Guang P. Optimizing the buckling strength of filament winding composite cylinders under hydrostatic pressure. *J. Reinf. Plast. Compos* 2018; 37: 892–904.

50. Herakovich CT. *Mechanics of fibrous composites*. University of Virginia, USA: Wiley, 1998.

51. Almeida JHS, Jr, Ribeiro ML, Tita V, et al. Damage modeling for carbon fiber/epoxy filament wound composite tubes under radial compression. *Compos. Struct* 2017; 160: 204–210.

52. Kachanov L. *Introduction to continuum damage mechanics*. USA: Springer Science & Business Media, 1986.

53. Zhu G, Sun G, Yu H, et al. Energy absorption of metal, composite and metal/composite hybrid structures under oblique crushing loading. *Int. J. Mech. Sci* 2018; 135: 458–483.

54. Baker C, Morscher GN, Pujar VV, et al. Transverse cracking in carbon fiber reinforced polymer composites: Modal acoustic emission and peak frequency analysis. *Compos Sci Technol* 2015; 116: 26–32.